Postprint of: Bazmara M., Sauer R., Agrawal A., Biomimetic torene shells, MATHEMATICS AND MECHANICS OF SOLIDS, Vol. 28, iss. 8 (2023), pp. 1926-1935
 DOI: 10.1177/10812865221146743

Mathematics and Mechanics of Solids
1–10

DOI: 10.1177/10812865221146743
journals.sagepub.com/home/mms

Biomimetic torene shells

Maziyar Bazmara
Department of Mechanical Engineering, University of Houston, Houston, TX, USA

Roger A Sauer
Department of Civil Engineering, Gdańsk University of Technology, Gdańsk, Poland; Graduate School AICES, RWTH Aachen University, Aachen, Germany; Department of Mechanical Engineering, Indian Institute of Technology Guwahati, Guwahati, India

Ashutosh Agrawal
Department of Mechanical Engineering, University of Houston, Houston, TX, USA

Received 21 November 2022; accepted 6 December 2022

Abstract
The genome inside the eukaryotic cells is guarded by a unique shell structure, called the nuclear envelope (NE), made of lipid membranes. This structure has an ultra torus topology with thousands of torus-shaped holes that imparts the structure a high flexural stiffness. Inspired from this biological design, here we present a novel "torene" architecture to design lightweight shell structures with ultra-stiffness for engineering applications. We perform finite element analyses on classic benchmark problems to investigate the mechanics of torene shells. This study reveals that the torene shells can achieve one order of magnitude or higher flexural stiffness than traditional shells with the same amount of material. This novel geometric strategy opens new avenues to exploit additive manufacturing to design lightweight shell structures for extreme mechanical environments.

Keywords
Shell structures, architected material, flexural stiffness, finite element analysis, topology

1. Introduction

Shell structures have been used for centuries in diverse fields of engineering due to their ability to support large loads with a thin architecture. The examples are abundant, ranging across a wide spectrum such as the Sydney Opera House or the fuselages of aircrafts at large length scales, to soccer balls and egg cartons at smaller length scales. Examples of shell structures are also abundant in organic structures. The skulls and bones in our body are shell structures. Going to cellular scales, the physical enclosures of the biological cells and their organelles, as well as the bacteria and virus, are all shell structures. One specific cellular structure that is responsible to guard the genome is the nuclear envelope (NE), the

Corresponding author:
Ashutosh Agrawal, Department of Mechanical Engineering, University of Houston, 4226 Martin Luther King Boulevard, Houston, TX 77204, USA.
Email: ashutosh@uh.edu

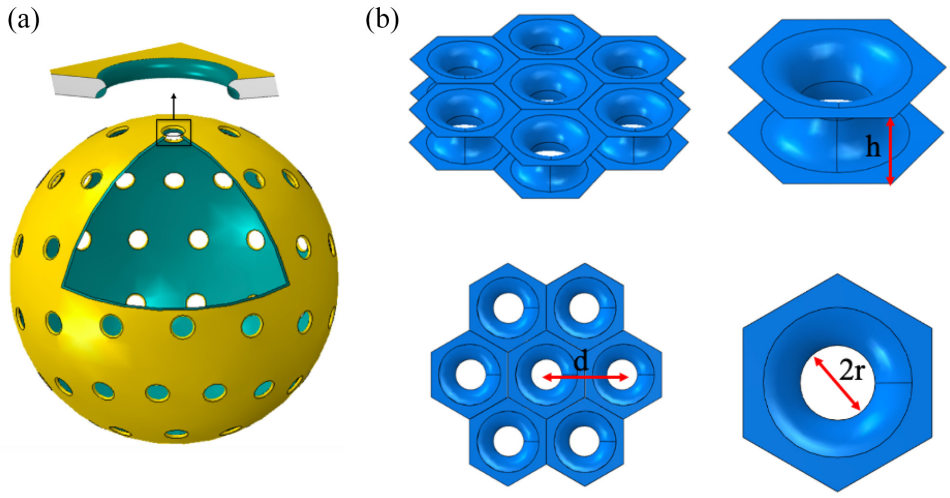

Figure 1. Biomimetic architecture of torene shells. (a) A schematic of an idealized geometry of the nuclear envelope in eukaryotic cells. Thousands of torus-shaped holes connect the two concentric lipid bilayer shells. (b) The design elements of the proposed torene shells inspired from the nuclear envelope geometry. The torene shells are characterized by inter-surface separation h, inter-hole separation d, and the hole radius at the midplane r.

boundary of the cell nucleus. The NE is made of lipid membranes which behave as two-dimensional (2D) fluid shells [1–5]. It has a unique topology comprising of two concentric hollow shells fused at thousands of sites with torus (or donut) shaped holes (Figure 1(a)) [6,7]. This imparts NE, a genus on the order of thousands. We studied the consequences of the architecture on the mechanical properties of this ultra torus structure. Using curvature elasticity for fluid membranes, this study performed on a single hole with double membranes revealed that the double membrane structure possesses one order of magnitude higher flexural stiffness than a single membrane [8].

Inspired from our findings, in this study, we propose a new class of biomimetic shell structures, which we have named torenes. This class of structures comprises of concentric shell layers that are fused via torus-shaped holes (Figure 1(b)). We perform benchmark tests [9] to characterize the mechanical strength of the torene cylinders and torene domes using finite element simulations. In comparison with previous studies [6–8], these structures have curved macroscopic geometries, possess a high genus (determined by the number of holes), and are made of elastic solid materials. We compare their flexural stiffness to solid cylinders and domes with equivalent mass. Our analysis reveals that the torene structures exhibit one order of magnitude or higher flexural stiffness than the corresponding solid cylinders and solid domes for a wide range of design parameters. These torene shell structures could provide novel ways to design lightweight structures across length scales for countering extreme mechanical loads.

2. Method

We performed finite element simulations to test the mechanical performance of the torene structures. We analyzed two types of torene structures: open-ended cylinders and hemispherical domes. The layers in the torene structures were connected to each other via torus-shaped holes with negative Gaussian curvature (Figure 1(b)). The holes are placed in a hexagonal pattern. The torus architecture is defined by the separation between the parallel surfaces (h), separation between the holes (d), and the radius of the torus hole at the midplane (r). We used the finite element software package ABAQUS to perform the simulations [10]. To avoid jumps in curvatures, we applied the built-in curvature continuity feature in Dassault Systèmes SOLIDWORKS. To mesh the structures, we used the three-node triangular general-purpose shell element S3 [10] to model the proposed torene architectures with a global approximate element size of 0.2 μm. The S3 element is a general-purpose shell element that is capable of providing solutions to both thin and thick shell problems using rotational degrees of freedom. All shell elements use bending strain measures based on the Koiter–Sanders shell theory [11]. The transverse shear treatment

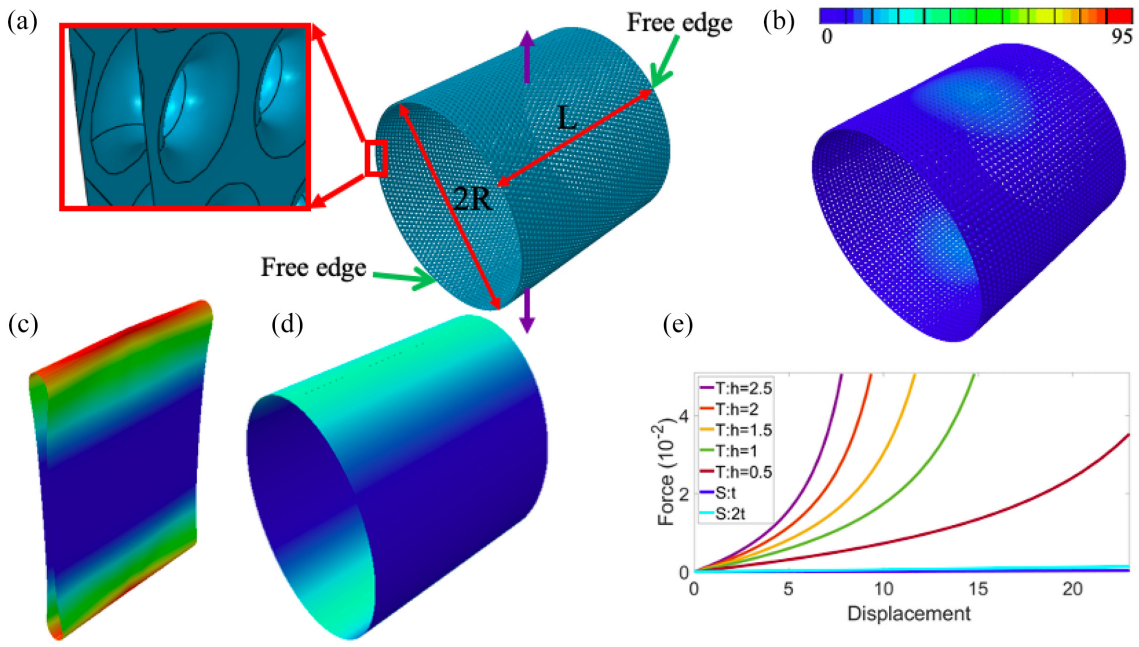

Figure 2. Flexural response of torene cylinder under tensile load. (a) Architecture of the torene cylinder. The inset shows the torus holes. The cylinder is subjected to tensile point loads, and the circular edges of the cylinder are traction free. (b–d) Deformed geometries of the torene cylinder, solid cylinder with thickness t, and solid cylinder with thickness $2t$, respectively. All the deformed shapes correspond to a force of 5.05×10^{-2}. (e) Force–displacement curves for torene cylinders with different inter-surface separation for $d = 5$, $R = 100$, $L = 200$, and the two solid cylinders.
The color scale in (b) and the x-axis in (e) show the vertical displacements normalized with respect to $r = 1$ μm, and the radius of the torus hole. The force is normalized with respect to Er^2, where $E = 10$ MPa.

is based on the linear theory by MacNeal [12,13] and Hughes and Tezduyar [14], and the nonlinear theory by Simo et al. [15]. The constitutive model of the S3 element is based on the theory of hypoelasticity [10].

We used nonlinear kinematics within ABAQUS/Standard, which allows the thickness of the finite strain shell elements to vary as a function of the effective Poisson's ratio. We performed transient analysis where the kinetic energy was less than 5% of the total strain energy in order to ensure quasi-static conditions. All the force-deformation simulations were performed under load control. Both the torene and solid structures were modeled with isotropic linear elastic material properties with a Young's modulus of 10 MPa (E), Poisson's ratio of 0.3125 (ν), and a density of 750 kg/m^3 (ρ). A single layer of the torene structure had a thickness (t) of 0.1 μm. The solid cylinders and solid domes were with thicknesses of t and $2t$, to allow comparisons of flexural stiffnesses.

3. Results

3.1. Cylinder subjected to tensile point loads

Figure 2(a) shows the geometry of one of the simulated torene cylinders. The inset shows a zoomed-in view of the torus holes that connect the two surfaces. We prescribed a radius of $r = 1$ μm for the torus holes at the midplane for all the simulated cases. We used this length scale to normalize all the dimensions discussed in this study. Using this metric, the cylinder shown in Figure 2(a) has a mean radius of $R = 100$, length of $L = 200$, inter-hole separation of $d = 5$, inter-surface separation of $h = 2$, and a surface thickness of $t = 0.1$. The cylinder is subjected to tensile point forces on the opposite points as shown in the figure. We simulated a set of torene cylinders with h varying from 0.5 to 2.5 at an increment of 0.5 and l varying from 5 to 9 at an increment of 1. We also simulated solid cylinders with thickness t and $2t$ (same R and L) to compare their flexural stiffnesses with that of torene cylinders.

(a)

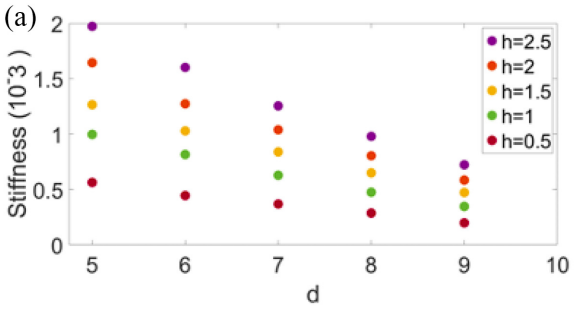

(b)

RA	h=2.5	h=2	h=1.5	h=1	h=0.5
d=5	22.5	19.5	14.4	9.7	5.1
d=6	18.6	15.1	10.7	6.8	3.5
d=7	14.5	11.5	8.0	5.3	2.7
d=8	10.9	8.8	5.9	3.8	2.1
d=9	8.5	7.5	4.8	2.9	1.9

Figure 3. Torene cylinders under tensile load exhibit high flexural stiffness. (a) Stiffness of torene cylinders in tension for $d = 5$. The slopes are taken from the initial linear regime of the force–displacement curves. (b) Ratio of amplification (RA), which is the ratio of the stiffness of the torene cylinder with respect to the stiffness of the solid cylinder with thickness $2t$. The green highlighted fields indicate the geometric parameters of the torene cylinders that yield at least one order of magnitude or higher amplification in flexural stiffness.
d and h are normalized with respect to $r = 1$ μm, and the stiffness is normalized with respect to Er, where $E = 10$ MPa.

Figure 2(b)–(d) shows the deformed geometries of the torene and two solid cylinders with thickness t and $2t$, respectively, at a normalized force of 5.05×10^{-2}. The force is normalized with respect to Er^2, where $E = 10$ MPa. The figures show that the solid cylinders undergo much higher deformation than the torene cylinders, demonstrating that the torene cylinders possess a much higher flexural stiffness. Figure 1(e) shows the force–displacement response of torene cylinders for $l = 5$ and different h values and the solid cylinders. The plots reveal that the torene cylinders require much higher forces to deform than the solid cylinders. The force–deformation response of the solid cylinders remains linear in the simulated high deformation regime, whereas the torene plots become nonlinear with a significant increase in the stiffnesses.

To estimate the effectiveness of torene architecture in resisting bending deformations, we computed the stiffness from the initial linear regime of the force–displacement curves. Figure 3(a) shows these stiffnesses for different h values as a function of d. The stiffnesses of the torene cylinders reduce with an increase in d, and increase with an increase in h. This suggests that the flexural stiffness increases with increasing inter-surface separation and increasing density of torus holes. We then computed a ratio of amplification (RA) defined by the ratio of the stiffness of the torene cylinder to the stiffness of the solid cylinder with $2t$ thickness, to quantify the enhancement in flexural stiffness provided by the torene architecture. Figure 3(b) shows a table with RA as a function of h and d. The lowest amplification is 2 for the smallest separation ($h = 0.5$) and the lowest hole density ($d = 9$) simulated. The largest amplification is 22.5 for the largest separation ($h = 2.5$) and the largest hole density ($d = 5$) simulated. The green highlighted region in the table indicates the $\{h, d\}$ values that yield one order of magnitude or higher amplification in flexural stiffness. It is important to note that this amplification in stiffness is achieved with respect to the solid cylinder with equivalent mass (thickness $2t$).

3.2. Cylinder subjected to compressive point loads

The second benchmark simulation we performed considers a cylinder subjected to compressive point loads (Figure 4(a)). The torene cylinders and the solid cylinders have the same geometry as before. However, the cylinders now have rigid diaphragms at the open ends, which restrict the in-plane displacements at the open ends. Rigid diaphragm boundary conditions are enforced by fixing all nodal displacement components lying within the plane of the diaphragm. The deformed shapes of the torene cylinder and the solid cylinders at a normalized compressive force of 5.90×10^{-3} are shown in Figure 4(b)–(d). These shapes again show that the solid cylinders undergo much larger deformation than the torene cylinders. The force–deformation response again reveals that the torene cylinders require much larger forces than the solid cylinders to deform by the same amount. The solid cylinders still show a linear response within the considered range of deformation.

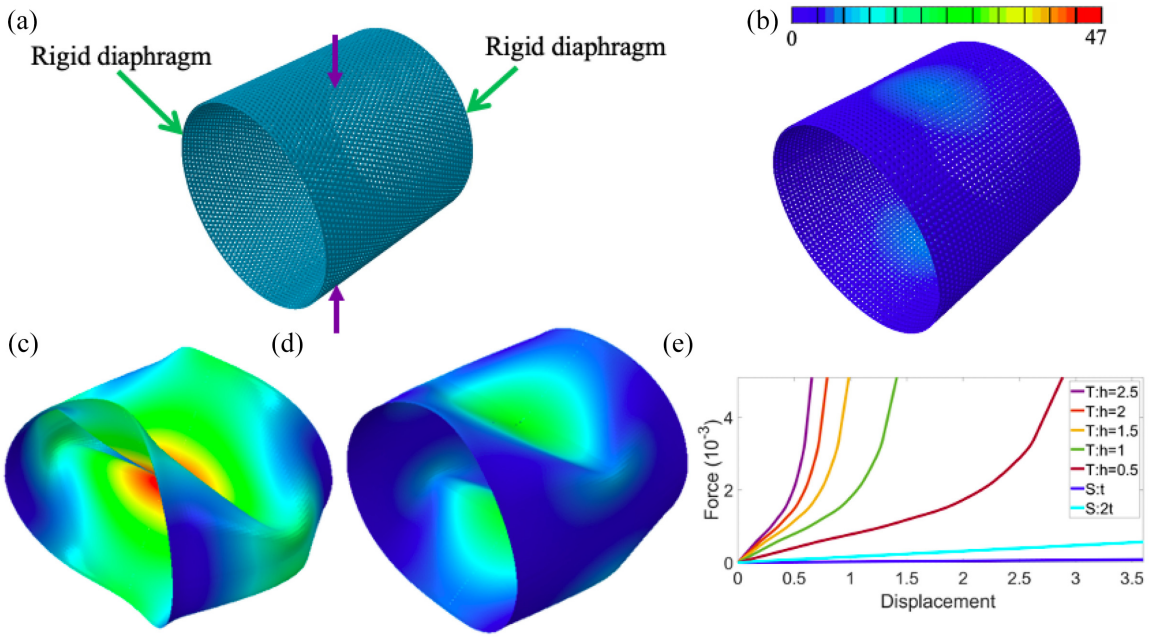

Figure 4. Flexural response of torene cylinder under compressive load. (a) Architecture of the torene cylinder. The cylinder is subjected to compressive point loads and the circular edges of the cylinder have rigid diaphragm boundary conditions. (b–d) Deformed geometries of the torene cylinder, solid cylinder with thickness t, and solid cylinder with thickness $2t$. All the deformed shapes correspond to a force of 5.90×10^{-3}. (e) Force–displacement curves for torene cylinders with different inter-surface separation for $d = 5$, $R = 100$, $L = 200$, and the two solid cylinders.
The color scale in (b) and the x-axis in (e) show the vertical displacements normalized with respect to $r = 1$ μm. The force is normalized with respect to Er^2, where $E = 10$ MPa.

The stiffnesses from the initial linear phase of the force–deformation plots of the torene cylinders are plotted in Figure 5(a) as a function of h and d. The flexural stiffnesses of the torene cylinders decrease with a decrease in hole density and increase with an increase in the separation between the torene layers. The RA with respect to the solid cylinders with $2t$ thickness is shown in Figure 5(b). The RA varies between 5 and 41 for the simulated structures. We note that the amplification in compression reaches higher values than in tension. These results again show that there is a considerable design phase space of h and d, in which one order of magnitude or higher amplification if provided by torene architectures.

3.3. Effect of cylinder radii

Next, we analyzed the effect of radius (R) on the flexural stiffness of torene cylinders. In all the previous cases discussed so far, the cylinders had a radius of 100. Here, we reduced the radius and simulated samples with radii equal to 25, 50, and 75. We performed the tension and compression tests with the boundary conditions described in the previous sections. Figure 6(a) and (c) shows the deformed geometries of the torene and solid cylinders with a radius of 50 subjected to a tensile force of 5.05×10^{-2} and a compressive force of 5.90×10^{-3}, respectively. Figure 6(b) and (d) shows the force–deformation curves in tension and compression, respectively, for different radii. The torene plots (labeled T) are in solid, and the corresponding solid cylinder plots (labeled S) are in dashed lines. For all the cases, torenes require much larger forces than solid cylinders to achieve the same level of deformation. Figure 7(a) and (b) shows the stiffnesses of torene and solid cylinders estimated from the linear force–deformation regimes for tension and compression cases, respectively. The torene cylinders have higher stiffnesses than the corresponding solid cylinders, which are reflected in the RA values listed in Figure 7(c). The RA increases significantly, reaching double digit numbers, with a reduction in the radius of the cylinder.

(a)

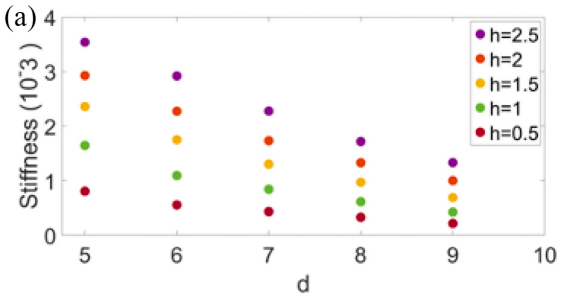

(b)

RA	h=2.5	h=2	h=1.5	h=1	h=0.5
d=5	40.8	34.8	28.5	21.4	13.4
d=6	31.6	27.2	21.1	15.9	9.6
d=7	24.7	22.2	17.2	12.9	8.0
d=8	19.3	17.3	13.3	9.9	6.2
d=9	15.7	13.7	10.6	8.0	4.7

Figure 5. Torene cylinders under compressive load exhibit high flexural stiffness. (a) Stiffness of torene cylinders in compression for $d = 5$. The slopes are calculated from the initial linear regime of the force–displacement curves. (b) Ratio of amplification (RA), which is the ratio of the stiffness of the torene cylinder with respect to the stiffness of the solid cylinder with thickness $2t$. The green highlighted fields indicate the geometric parameters of the torene cylinders that yield one order of magnitude or higher amplification in flexural stiffness.

d and h are normalized with respect to $r = 1$ μm, and the stiffness is normalized with respect to Er, where $E = 10$ MPa.

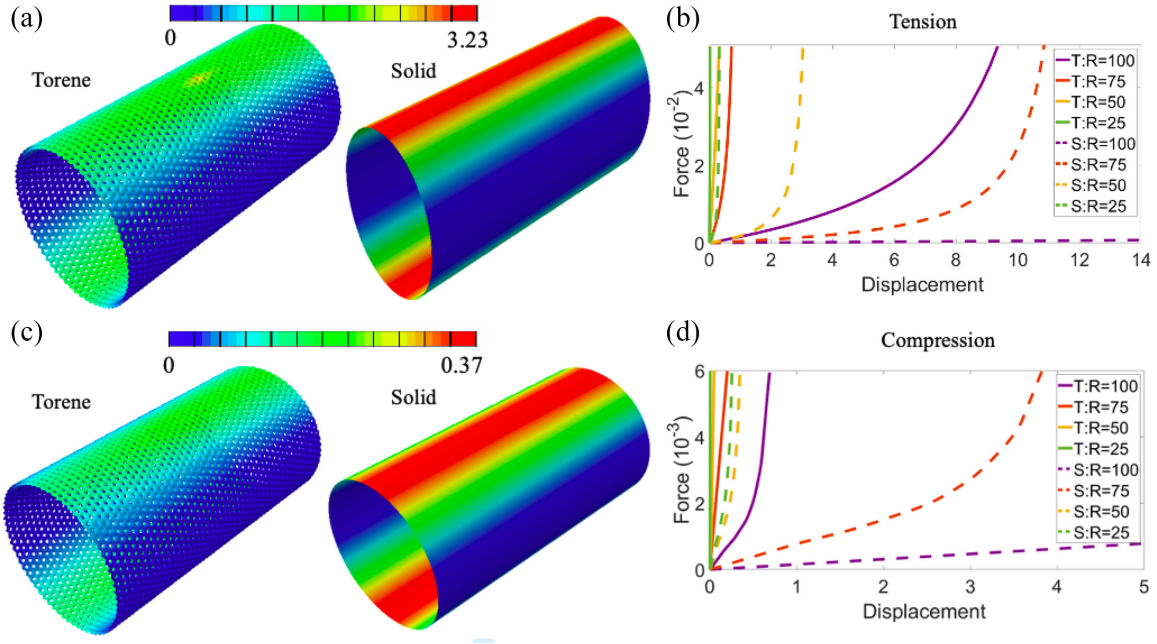

Figure 6. Flexural response of torene cylinders with different radii under tensile and compressive loads. (a) Deformed geometry of the torene cylinder and solid cylinder (thickness $2t$) with $R = 50$ under a tensile point load of 5.05×10^{-2}. (b) Force–displacement curves for the torene cylinders and the solid cylinders (thickness $2t$) under tensile loads. (c) Deformed geometry of the torene cylinder and solid cylinder (thickness $2t$) with $R = 50$ under a compressive point load of 5.90×10^{-3}. (d) Force–displacement curves for the torene cylinders and the solid cylinders (thickness $2t$) under compressive loads.

The color scales in (a) and (c) and the x-axis in (b) and (d) show the vertical displacements normalized with respect to $r = 1$ μm. The forces in (b) and (d) are normalized with respect to Er^2, where $E = 10$ MPa.

3.4. Hemispherical dome subjected to tensile and compressive point loads

The final benchmark problem considers a hemispherical dome with a 18° cutout at the pole region subjected simultaneously to compressive and tensile forces as shown in Figure 8(a). The torene domes have d varying from 5 to 9 at an increment of 1, and h varying from 0.5 to 2.5 at an increment of 0.5. Figure 8(b)–(d) shows the deformed shapes of the torene domes, and the corresponding solid domes with

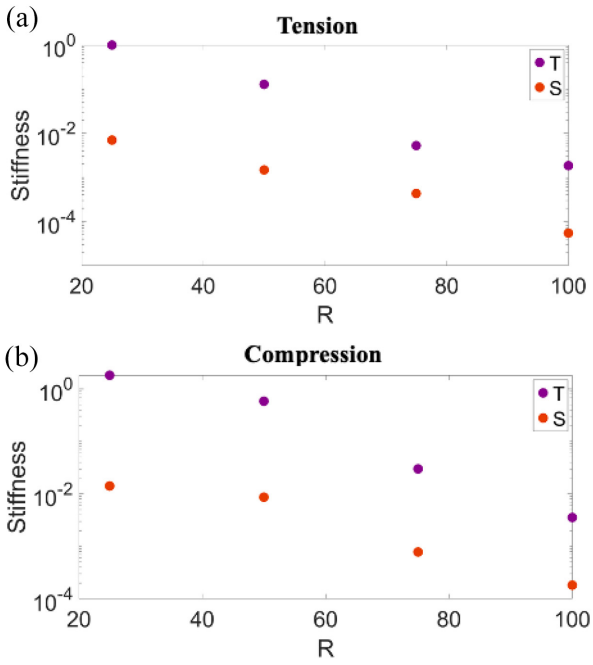

(c)

RA	Tension	Compression
R=100	34.8	19.5
R=75	56.7	38.4
R=50	87.3	72.6
R=25	143.1	129.2

Figure 7. Torene cylinders with varying radii exhibit high flexural stiffness. (a) Stiffness of torene cylinders in tension for $d = 5$ and $h = 2$. (b) Stiffness of torene cylinders in compression for $d = 5$ and $h = 2$. (c) Ratio of amplification (RA) for torene cylinders with respect to solid cylinders with thickness $2t$. All the simulated torene cylinders show one order of magnitude or higher amplification in flexural stiffness (green highlighted region).
R is normalized with respect to $r = 1$ μm, and the stiffness is normalized with respect to Er, where $E = 10$ MPa.

thickness t and $2t$, subjected to a force of 4.95×10^{-3} at points A and B. The solid domes undergo much larger deformation than the torene domes, again demonstrating that the torene dome is much more resilient to bending than the solid domes.

Figure 8(e) and (f) shows the force–displacement plots at points A and B. The stiffnesses from the linear regime are presented in Figure 9(a) and (c) for points A and B, respectively. The stiffnesses decrease with an increase in d, and increase with an increase in h. The RA based on the stiffnesses obtained from points A and B is presented in Figure 9(b) and (c). As for cylinders, torene domes exhibit an order of magnitude or higher amplification in the flexural stiffness in a considerable phase space (indicated by the highlighted green region).

4. Discussion

In this study, we propose a new design of bioinspired shell structures, called torene shells. These shells are characterized by more than one concentric layer, connected by torus-shaped holes. We perform benchmark tests on cylinder and dome shells to test the flexural response of torene architecture. This study reveals that the torene shells can offer more than one order of magnitude or higher magnification in flexural stiffness for nearly the same mass of material compared to solid shells in a large design space. Our findings are length scale and material properties independent, and therefore suggest that the torene architecture could be used to design lightweight shell structures for extreme environments in diverse set-ups. For any arbitrary mass of the material, a torene structure will yield an amplification in the flexural stiffness compared to the counterpart solid structure under quasi-static loads. Our work adds a new class of material to the growing list of architected materials that offer mechanical advantages [16–19].

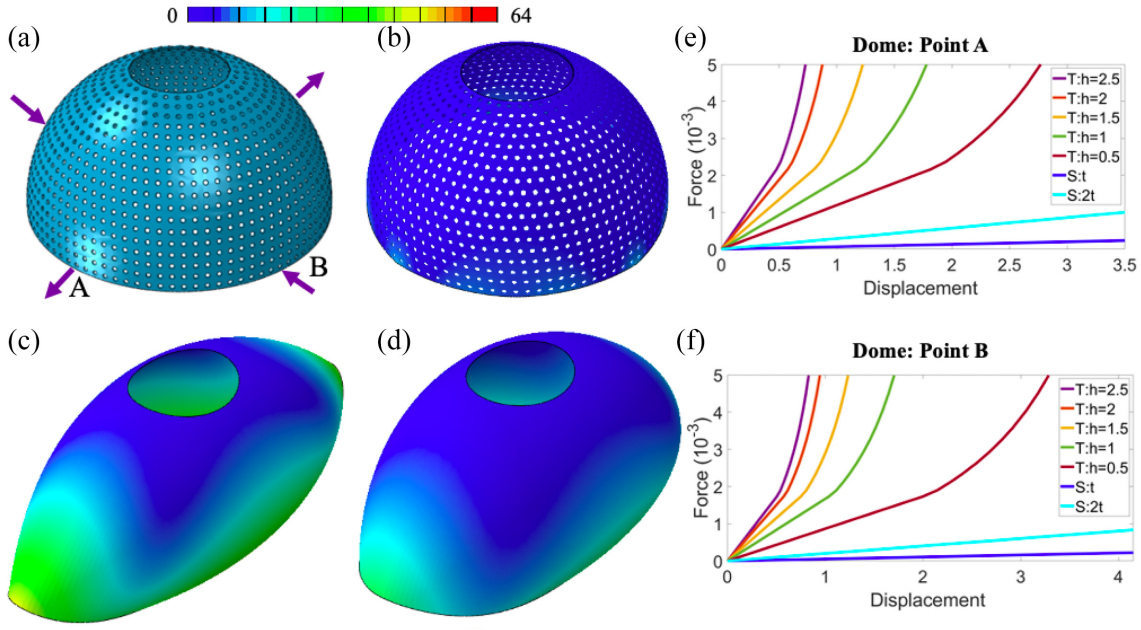

Figure 8. Flexural response of torene dome under tensile and compressive loads. (a) Architecture of the torene dome. The dome has a 18° cutout at the pole. The dome is subjected to tensile point loads at A and compressive point loads at B. (b–d) Deformed geometries of the torene dome, solid dome with thickness t, and solid dome with thickness $2t$. All the deformed shapes correspond to a force of 4.95×10^{-3} at points A and B. (e and f) Force–displacement curves for torene domes with different inter-surface separation for $d = 5$, $R = 100$, and the two solid domes, at points A and B, respectively.
The color scale in (a) and the x-axis in (e) and (f) show vertical displacements normalized with respect to $r = 1$ μm. The force is normalized with respect to Er^2, where $E = 10$ MPa.

The RA computed from stiffnesses in the linear regime can be understood from the notion of the second moment of area. For a one-dimensional (1D) beam with a rectangular cross, width b, thickness $2t$, and the second moment of area is given by:

$$I_s = \frac{2bt^3}{3}. \tag{1}$$

If we distribute this material into two rectangular sections spaced h distance apart from each other (center-to-center) and invoke the parallel axis theorem, the second moment of area for the torene structure would become:

$$I_t = 2\left(\frac{bt^3}{12} + \frac{bth^2}{4}\right), \tag{2}$$

where the first part is negligible for $t \ll h$. Thus, in the absence of any other differences, the RA in the flexural stiffness is given by the ratio of second moment of area:

$$\mathrm{RA} = \frac{I_t}{I_s} \approx \frac{3}{4}\left(\frac{h}{t}\right)^2. \tag{3}$$

For $h/t = 10$ used in this study, the theoretical limit for RA, therefore, comes out to be 75. The majority of the RAs presented in this study fall below this theoretical estimate. The only case where the RA values exceed this is in the case of torene cylinders with small radii. In the future, it would be insightful to study large deformations and stability of torene structures under different loading conditions such as in-plane loading, out-of-plane loading, and combined loading. It would then be valuable to study critical loads, and characterize the geometric features of local buckles. As the torene structures

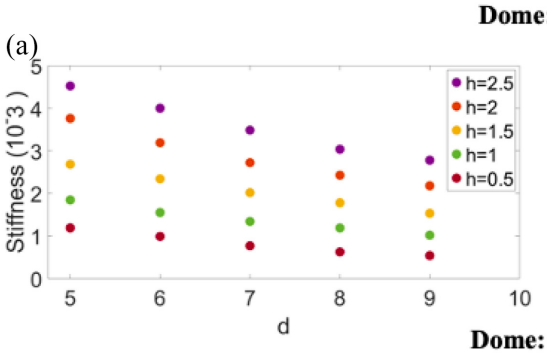

(b)

RA	h=2.5	h=2	h=1.5	h=1	h=0.5
d=5	15.8	14.6	10.4	7.2	4.6
d=6	14.1	12.3	9.1	6.0	3.9
d=7	12.2	10.5	7.8	5.2	2.9
d=8	10.6	9.4	6.9	4.6	2.4
d=9	9.7	8.4	5.9	3.9	2.1

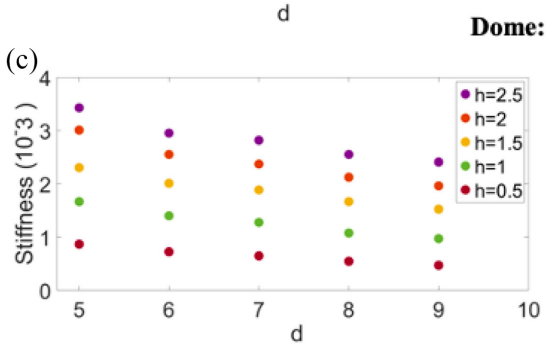

(d)

RA	h=2.5	h=2	h=1.5	h=1	h=0.5
d=5	17.0	15.4	11.7	8.5	4.4
d=6	14.7	13.0	10.3	7.1	3.9
d=7	13.3	11.4	9.1	6.2	3.2
d=8	12.7	10.8	8.5	5.5	2.8
d=9	11.9	10.1	7.9	4.9	2.4

Figure 9. Torene domes exhibit high flexural stiffness. (a) Stiffness of torene domes ($d = 5$) obtained from the initial linear regime of the force–displacement curves computed for point A. (b) Ratio of amplification of the torene domes with respect to the stiffness of the solid domes with thickness $2t$ obtained from stiffness values corresponding to point A. (c) Stiffness of torene domes ($d = 5$) obtained from the initial linear regime of the force–displacement curves computed for point B. (d) Ratio of amplification of the torene domes with respect to the stiffness of the solid domes with thickness $2t$ obtained from stiffness values corresponding to point B. The green highlighted fields in (b) and (c) show the geometric parameters of the torene cylinders that yield one order of magnitude or higher amplification in flexural stiffness.
d and h are normalized with respect to $r = 1$ μm, and the stiffness is normalized with respect to Er, where $E = 10$ MPa.

are made up of coexistent regions with varying Gaussian curvatures, the emergence of local faceted structures and nonlocal deformations [20] could exhibit a complex behavior. Also, it would be useful to study the optimization principles to identify the topologies that yield desired resilience for different types of mechanical loads. For example, while increasing the inter-surface separation enhances flexural stiffness, it could lead to buckling of torus holes under normal compressive loads. Thus, it is essential to investigate performance-dependent optimal torene structures in future studies.

Acknowledgements

The authors acknowledge Dr Mehdi Torbati, Dr Ehsan Irajizad, and Dr Carlos Osorio for scientific discussions.

Funding

The author(s) disclosed receipt of the following financial support for the research, authorship, and/or publication of this article: A.A. acknowledges support from the National Science Foundation (NSF) grants CMMI-1727271 and CMMI-1931084.

ORCID iDs

Maziyar Bazmara https://orcid.org/0000-0002-0362-8325
Roger A Sauer https://orcid.org/0000-0001-5625-8295
Ashutosh Agrawal https://orcid.org/0000-0002-9923-8603

References

[1] Jenkins, JT. Static equilibrium configurations of a model red blood cell. *J Math Biol* 1977; 4(2): 149–169.
[2] Steigmann, D. Fluid films with curvature elasticity. *Arch Ration Mech Anal* 1999; 150(2): 127–152.
[3] Steigmann, D, Baesu, E, Rudd, RE, et al. On the variational theory of cell-membrane equilibria. *Interf Free Bound* 2003; 5(4): 357–366.
[4] Agrawal, A, and Steigmann, DJ. Boundary-value problems in the theory of lipid membranes. *Contin Mech Thermodyn* 2009; 21(1): 57–82.
[5] Sauer, RA, Duong, TX, Mandadapu, KK, et al. A stabilized finite element formulation for liquid shells and its application to lipid bilayers. *J Comput Phys* 2017; 330: 436–466.
[6] Torbati, M, Lele, TP, and Agrawal, A. Ultradonut topology of the nuclear envelope. *Proc Natl Acad Sci* 2016; 113(40): 11094–11099.
[7] Agrawal, A, and Lele, TP. Mechanics of nuclear membranes. *J Cell Sci* 2019; 132(14): 229245.
[8] Agrawal, A, and Lele, TP. Geometry of the nuclear envelope determines its flexural stiffness. *Mol Biol Cell* 2020; 31(16): 1815–1821.
[9] Sze, K, Liu, X, and Lo, S. Popular benchmark problems for geometric nonlinear analysis of shells. *Fin Elem Anal Des* 2004; 40(11): 1551–1569.
[10] Simulia, Inc. Abaqus 6.14 documentation, http://130.149.89.49:2080/v6.14/
[11] Budiansky, B. *On the "best" first-order linear shell theory* (The Prager anniversary volume: progress in applied mechanics). New York: MacMillan, 1963.
[12] MacNeal, RH. A simple quadrilateral shell element. *Comput Struct* 1978; 8(2): 175–183.
[13] MacNeal, RH. Derivation of element stiffness matrices by assumed strain distributions. *Nucl Eng Des* 1982; 70(1): 3–12.
[14] Hughes, TJ, and Tezduyar, T. Finite elements based upon mindlin plate theory with particular reference to the four-node bilinear isoparametric element. *J Appl Mech* 1981; 48: 587–596.
[15] Simo, JC, Fox, DD, and Rifai, MS. On a stress resultant geometrically exact shell model. Part III: computational aspects of the nonlinear theory. *Comput Meth Appl Mech Eng* 1990; 79(1): 21–70.
[16] Qin, Z, Jung, GS, Kang, MJ, et al. The mechanics and design of a lightweight three-dimensional graphene assembly. *Sci Adv* 2017; 3(1): e1601536.
[17] Senhora, FV, Sanders, ED, and Paulino, GH. Optimally-tailored spinodal architected materials for multiscale design and manufacturing. *Adv Mater* 2022; 34: 2109304.
[18] Liu, K, Pratapa, PP, Misseroni, D, et al. Triclinic metamaterials by tristable origami with reprogrammable frustration. *Adv Mater* 2022; 34: 2107998.
[19] Portela, CM, Edwards, BW, Veysset, D, et al. Supersonic impact resilience of nanoarchitected carbon. *Nat Mater* 2021; 20(11): 1491–1497.
[20] Vaziri, A, and Mahadevan, L. Localized and extended deformations of elastic shells. *Proc Natl Acad Sci* 2008; 105(23): 7913–7918.